BULLETIN OF THE POLISH ACADEMY OF SCIENCES
TECHNICAL SCIENCES, Vol. 61, No. 1, 2013
DOI: 10.2478/bpasts-2013-0007

Computational modelling of concrete behaviour under static and dynamic conditions

I. MARZEC* and J. TEJCHMAN

Faculty of Civil and Environmental Engineering, Gdańsk University of Technology,
11/12 Narutowicza St., 80-233 Gdańsk-Wrzeszcz, Poland

Abstract. The paper presents results of FE simulations of the concrete behaviour under quasi-static and dynamic loading. For quasi-static cyclic analyses, an enhanced coupled elasto-plastic-damage constitutive model has been used. To take the effect of the loading velocity into account, viscous and inertial terms have been also included. To ensure the mesh-independence and to properly reproduce strain localization in the entire range of strain rates, a constitutive formulation has been enhanced by a characteristic length of micro-structure by means of a non-local theory. Numerical results have been compared with some corresponding laboratory tests.

Key words: concrete, damage mechanics, dynamic loading, elasto-plasticity, non-local theory, viscosity.

1. Introduction

A fracture process is a fundamental phenomenon in quasi-brittle materials like concrete [1]. At the beginning of the loading, regions with several micro-cracks are formed. Later these micro-cracks create macro-cracks. Thus, a fracture process is subdivided in general into two main stages: appearance of narrow regions of intense strain deformation with a certain volume (including micro-cracks) and occurrence of discrete macro-cracks [2]. Within continuum mechanics, strain localization can be numerically captured by a continuous approach and discrete macro-cracks by a discontinuous one. Usually, to describe the fracture behaviour of concrete, one approach is used. However, in order to describe the entire fracture process, a continuous approach should be connected with a discontinuous one [3]. The description of fracture is crucial to evaluate the material strength at peak and in the post-peak regime. Fracture strongly depends among others on the loading type (monotonic or cyclic), loading velocity (quasi-static or dynamic) and moisture level. Thus, concrete is a highly rate-dependent material [4–6].

The aim of our research works is to develop a reliable phenomenological constitutive model for concrete under dynamic loading for practical engineering applications. The results in the paper show: 1) the capability of a coupled elasto-plastic-damage continuum model to describe a quasi-static monotonic and cyclic concrete behaviour at macro-level and 2) the capability of an elasto-visco-plastic continuum model to describe the concrete behaviour under dynamic conditions at macro-level (micro-structural phenomena at aggregate level during fracture were not considered). The constitutive models were enhanced by a characteristic length of micro-structure by means of a non-local theory in order to capture strain localization. Numerical results were compared with some corresponding laboratory tests.

2. Constitutive model for concrete under quasi-static conditions

An analysis of concrete elements under cyclic loading is complex mainly due to their stiffness degradation caused by cracks [7–9]. To take into account a reduction of the concrete strength, irreversible (plastic) strains and stiffness degradation, a combination of plasticity and damage theories is physically very appealing since plasticity considers the first two properties and damage takes into account a loss of the material strength and the stiffness deterioration. An improved coupled elasto-plastic-damage model has been proposed based on the formulation by Pamin and de Borst [10], which combines elasto-plasticity with a scalar damage assuming a strain equivalence hypothesis. The elasto-plastic deformation has been defined in terms of effective stresses according to a general relationship

$$f_p = F\left(\sigma_{ij}^{eff}\right) - \sigma_y\left(\kappa_p\right), \tag{1}$$

wherein F – the plastic failure function defined in effective stresses σ_{ij}^{eff}, σ_y – the uniaxial tension yield stress, and κ_p – the hardening/softening parameter equal to the plastic strain in uniaxial tension/compression. Two criteria were used in a plastic regime: the linear Drucker-Prager criterion with a non-associated flow rule in compression and the Rankine criterion with an associated flow rule in tension [11–12] defined by effective stresses

$$\sigma_{ij}^{eff} = C_{ijkl}^{e}\varepsilon_{kl}. \tag{2}$$

The yield surface based on a linear Drucker-Prager criterion was assumed in the following form

$$f_1 = q + p\tan\varphi - \left(1 - \frac{1}{3}\tan\varphi\right)\sigma_{yc}\left(\kappa_1\right), \tag{3}$$

where q – the Mises equivalent deviatoric stress, p – the mean stress and φ – the internal friction angle. The material hard-

*e-mail: irek@pg.gda.pl

ening/softening has been defined by the uniaxial compression stress $\sigma_{yc}(\kappa_1)$, wherein κ_1 is the hardening-softening parameter. A simplified linear Drucker-Prager criterion is not usually suitable in a compression regime if high pressure is concerned, because it is not able to correctly describe a pressure sensitivity of concrete materials (a curved criterion should be used). The flow potential was

$$g_1 = q + p\tan\psi \tag{4}$$

with the dilatancy angle $\psi \neq \varphi$. In turn, in the tensile regime, a Rankine criterion was used including a yield function f_2 with isotropic softening defined as [11, 12]

$$f_2 = \max\{\sigma_1, \sigma_2, \sigma_3\} - \sigma_{yt}(\kappa_2), \tag{5}$$

where σ_i – the principal stresses, σ_{yt} – the tensile stress and κ_2 – the softening parameter. Next, the material degradation has been calculated within damage mechanics, independently in tension and compression based on the equivalent strain measure by Mazars [13] (ε_i – principal strains)

$$\widetilde{\varepsilon} = \sqrt{\sum_i \langle\varepsilon_i\rangle^2}. \tag{6}$$

In tension, the standard exponential evolution function was chosen for the damage parameter D

$$D_t = 1 - \frac{\kappa_0}{\kappa}\left(1 - \alpha + \alpha e^{-\beta(\kappa-\kappa_0)}\right), \tag{7}$$

wherein α and β are the material parameters. In turn, in compression, the function proposed by Geers [14] was adopted for the damage parameter evolution

$$D_c = 1 - \left(1 - \frac{\kappa_0}{\kappa}\right)\left(0.01\frac{\kappa_0}{\kappa}\right)^{\eta_1} - \left(\frac{\kappa_0}{\kappa}\right)^{\eta_2} e^{-\delta(\kappa-\kappa_0)}, \tag{8}$$

where η_1, η_2 and δ are the material constants. Equation (6) contributes to a differentiation of the stiffness degradation under tension and compression. Thus, damage under compression starts to develop later than under tension (that is consistent with experiments). The stresses were obtained according to

$$\sigma_{ij} = (1 - D)\,\sigma_{ij}^{\mathit{eff}}, \tag{9}$$

with the term '1-D' defined as follows [15]

$$(1 - D) = (1 - s_c D_t)(1 - s_t D_c), \tag{10}$$

and with two splitting functions s_c and s_t

$$s_c = 1 - a_c\left(1 - w\left(\boldsymbol{\sigma}^{\mathit{eff}}\right)\right) \quad \text{and} \quad s_t = 1 - a_t w\left(\boldsymbol{\sigma}^{\mathit{eff}}\right). \tag{11}$$

The factors a_t and a_c are the scale factors and $w\left(\boldsymbol{\sigma}^{\mathit{eff}}\right)$ denotes the stress weight function which may be determined with the aid of principal effective stresses [16]

$$w\left(\boldsymbol{\sigma}^{\mathit{eff}}\right) = \begin{cases} 0 & \text{if } \boldsymbol{\sigma} = 0 \\ \dfrac{\sum\left\langle\sigma_i^{\mathit{eff}}\right\rangle}{\sum\left|\sigma_i^{\mathit{eff}}\right|} & \text{otherwise} \end{cases}. \tag{12}$$

For relatively simple cyclic tests (e.g. uniaxial tension or bending), the scale factors a_t and a_c can be equal to $a_t = 0$ and $a_c = 1$, respectively. Thus, the splitting functions are: $s_t = 1$ and $s_c = w\left(\boldsymbol{\sigma}^{\mathit{eff}}\right)$. For uniaxial loading cases, the stress weight function becomes

$$w\left(\sigma^{\mathit{eff}}\right) = \begin{cases} 1 & \text{if } \sigma_{ii}^{\mathit{eff}} > 0 \\ 0 & \text{if } \sigma_{ii}^{\mathit{eff}} < 0 \end{cases}. \tag{13}$$

Thus, under pure tension the stress weight function $w = 1$ and under pure compression $w = 0$. Our constitutive model with a different stiffness in tension and compression and a positive-negative stress projection operator to simulate crack closing and crack re-opening is thermodynamically consistent. It shares main properties of the model by Lee and Fenves [16], which has been proved not to violate thermodynamic principles (plasticity is defined in the effective stress space, isotropic damage is used and the stress weight function is similar). Moreover, Carol and Willam [17] showed that for damage models with crack-closing-re-opening effects included, only isotropic formulations did not suffer from spurious energy dissipation under non-proportional loading (in contrast to anisotropic ones).

Our local coupled elasto-plastic-damage model requires the following 10 material constants E, ν, κ_0, α, β, η_1, η_2, δ, a_t, a_c and two hardening yield stress functions (the function by Rankine in tension and by Drucker-Prager in compression). If the tensile failure prevails, one yield stress function by Rankine can be used only. The quantities σ_y (presents in the hardening function) and κ_0 are responsible for the peak location on the stress-strain curve and a simultaneous activation of a plastic and damage criterion (usually the initial yield stress in the hardening $\sigma_{y0} = 3.5$–6.0 MPa and $\kappa_0 = (8$–$15)\times10^{-5}$ under tension). The shape of the stress-strain-curve in softening is influenced by the constant β in tension (usually $\beta = 50$–800), and by the constants δ and η_2 in compression (usually $\delta = 50$–800 and $\eta_2 = 0.1$–0.8). The parameter η_2 influences also a hardening curve in compression. In turn, the stress-strain-curve at the residual state is affected by the constant α (usually $\alpha = 0.70$–0.95) in tension and by η_1 in compression (usually $\eta_1 = 1.0$–1.2). Since the parameters α and η_1 are solely influenced by high values of κ, they can arbitrarily be assumed for softening materials. Thus, the most crucial material constants are σ_{y0}, κ_0, β, δ and η_2. In turn, the scale factors a_t and a_c influence the damage magnitude in tension and compression. In general, they vary between zero and one. There do not exist unfortunately the experimental data allowing for determining the magnitude of a_t and a_c. Since, the compressive stiffness is recovered upon the crack closure as the load changes from tension to compression and the tensile stiffness is not recovered due to compressive micro-cracks, the parameters a_c and a_t can be taken for the sake of simplicity as $a_c = 1.0$ and $a_t = 0$ for many different simple loading cases as e.g. uniaxial tension and bending. The equivalent strain measure can be defined in terms of total strains or elastic strains. The drawback of the presented formulation is the necessity to tune up constants controlling plasticity and damage to activate an elasto-plastic criterion and a damage criterion at the same moment. As a

consequence, the chosen initial yield stress σ_{y0} may be higher than this obtained directly in laboratory simple monotonic experiments. The material constants E, ν, κ_0, α, β, η_1, η_2, δ and two hardening yield stress functions can be determined for concrete with the aid of two independent simple monotonic tests: uniaxial compression test and uniaxial tension (or 3-point bending) test. However, the determination of the damage scale factors a_t and a_c requires one full cyclic compressive test and one full cyclic tensile (or 3-point bending) test.

3. Constitutive model for concrete under dynamic conditions

The concrete behaviour under both tension and compression strongly depends on the prescribed strain rate. The structural concrete resistance increases when the strain rate increases [18] due to 2 main reasons: inertia forces of micro-cracking and viscosity of free water in the capillary concrete system [18–26]. The first phenomenon is strongly affected by concrete fragmentation at high loading velocities [27, 28]. The material brittleness decreases and material fragmentation increases with increasing strain rate. During impact loading, the material post-peak behaviour can be very different [23]. The concrete strength after drying is less sensitive to loading rate.

Two different phases in the strength increase can be distinguished in compression and tension tests. In compression, the first phase corresponds to the strain rate $\dot{\varepsilon} < 10^{-1}$ 1/s (it leads to the maximum 1.5 – time increase of the compressive strength) and the second one to $\dot{\varepsilon} \geq 10^{-1}$ 1/s (it leads to the maximum 3-times increase of the compressive strength). In tension, two distinct phases also happen in the tensile strength increase. At $\dot{\varepsilon} = 10^{0}$ 1/s, the tensile strength is e.g. 2-times higher and at $\dot{\varepsilon} = 10^{2}$ 1/s is even 9-times greater. Consequently, the understanding the concrete behaviour within a very wide range of strain rates is fundamental. The concrete behaviour is experimentally at very high strain rates very difficult to be investigated since several different failure modes simultaneously at the macro- and meso-level occur.

An elastic-visco-plastic concrete model was developed based on an elasto-plastic criterion (the Drucker-Prager criterion in compression and Rankine criterion in tension, Sec. 2) enhanced by viscosity incorporated via the Duvaut–Lions overstress approach [29] (the stress state was allowed to remain outside the yield surface). The visco-plastic strain rate and hardening parameter were assumed as

$$\dot{\boldsymbol{\varepsilon}}^{vp} = \frac{1}{\tau}\left[\boldsymbol{C}^{e}\right]^{-1}\left(\boldsymbol{\sigma} - \overline{\boldsymbol{\sigma}}\right) \tag{14}$$

and

$$\dot{\kappa}^{vp} = \frac{1}{\tau}\left(\kappa - \overline{\kappa}\right), \tag{15}$$

where τ is the material parameter usually called relaxation time, $\overline{\boldsymbol{\sigma}}$ and $\overline{\kappa}$ are stress tensor and hardening/softening parameter of an inviscid material. The visco-plastic strain rate in Eq. (14) was simply equal to the difference between true stresses and stresses obtained in an inviscid material. The partition of the total strain rate into an elastic strain rate and a visco-plastic strain rate was assumed

$$\dot{\boldsymbol{\varepsilon}} = \dot{\boldsymbol{\varepsilon}}^{e} + \dot{\boldsymbol{\varepsilon}}^{vp}. \tag{16}$$

Such formulation allowed for a smooth transition from an inviscid to a viscous case (in contrast to an elasto-viscous-plastic approach by Perzyna [30]). A yield surface with an apex or a non-smooth surface could be used that was not possible in the model by Perzyna [30], wherein a yield surface had to be smooth with continuous stress derivatives in order to uniquely determine the direction of a visco-plastic strain rate. The first resolution of constitutive equations was carried out by considering the material as a rate-independent one, so the plastic stress tensor $\overline{\boldsymbol{\sigma}}$ and the hardening variable $\overline{\kappa}$ could be determined. In the second phase, the rate-dependency was incorporated with Eqs. (14) and (15). Finally, one obtained the updated viscoplastic stress Eq. (17) and the updated viscoplastic rate parameter Eq. (18) integrated over the time step Δt (from t up to $t + \Delta t$)

$$\boldsymbol{\sigma}_{n+1} = \frac{\left(\boldsymbol{\sigma}_n + \boldsymbol{C}^{e} : \Delta\boldsymbol{\varepsilon}\right) + \dfrac{\Delta t}{\tau}\overline{\boldsymbol{\sigma}}_{n+1}}{1 + \dfrac{\Delta t}{\tau}} \tag{17}$$

and

$$\kappa_{n+1} = \frac{\kappa_n + \dfrac{\Delta t}{\tau}\overline{\kappa}_{n+1}}{1 + \dfrac{\Delta t}{\tau}}. \tag{18}$$

A visco-plastic model by Duvant-Lions is quite convenient to be implemented, since a visco-plastic solution is the update of an inviscid solution [4]. A visco-plasticity produces in field equations a material length as a product of the elastic wave-speed times the relaxation time [29]. A local elasto-visco-plastic model requires the following four material constants to capture the elastic and plastic behaviour: E, ν, φ, ψ and two hardening/softening yield stress functions (the function by Rankine in tension and by Drucker–Prager in compression). These parameters can be easily determined with the aid of two independent simple monotonic tests for concrete: uniaxial compression test and uniaxial tension (or three-point bending) test. The determination of the viscous parameter τ requires several dynamic uniaxial compression and tension tests to capture the evolution of the strength increase factor at various strain rates.

4. Modelling of strain localization

To describe properly strain localization, to preserve the well-posedness of the boundary value problem, to obtain FE-results free from spurious discretization sensitivity and to capture a deterministic size effect (dependence of the nominal strength on the structure size), a integral-type non-local theory was used as a regularization technique [31–33]. It takes advantage of a weighted spatial averaging of a suitable state variable over a neighbourhood of each material point. Thus, a state

variable at a certain material point depends not only on the state variable at the point but on the distribution of the state variable in a finite neighbourhood of the point considered (the principle of a local action does not hold – a non-local interaction takes place between any two points). It has a physical motivation due to the fact the distribution of stresses in the interior of concrete at meso-scale is strongly non-uniform due to the presence of different phases (aggregate, cement matrix and bond). Polizzotto et al. [34] laid down a thermodynamic consistent formulation of non-local plasticity. In turn, Borino et al. [35] and Nguyen [36] proposed a thermodynamic consistent formulation of non-local damage.

Usually, in elasto-plastic formulations, it is sufficient to achieve mesh-independent FE results to treat non-locally one state variable controlling material softening (e.g. non-local softening parameter), whereas stresses, strains and other variables remain local [32, 37]. Similarly, in isotropic scalar damage models, it is sufficient to treat a variable describing material degradation as a non-local one [11]. However in other damage formulations, this variable has to be carefully chosen because a wrong choice can cause problems with energy dissipation leading to mesh-dependent FE solutions [38, 39]. When using a coupled elasto-plastic damage model with non-local softening (Sec. 2), the non-locality was applied to damage (since softening was not allowed in elasto-plasticity). The equivalent strain measure in Eq. (6) was replaced by its nonlocal counterpart:

$$\overline{\varepsilon}\left(x_k^a\right) = \int_V \omega\left(r\right) \widetilde{\varepsilon}\left(x_k\right) \mathrm{d}V, \tag{19}$$

where x_k^a – the coordinates of the considered (actual) point, x_k – the coordinates of the surrounding points, r – the distance between material points, ω – the weighting function and V – the body volume. In the case of an elasto-visco-plastic model (Sec. 3), the rates of the inviscid softening parameter $\overline{\kappa}$ (Eq. (15)) were averaged according to the schema by Brinkgreve [32]

$$\begin{aligned} \mathrm{d}\widetilde{\kappa}_i\left(x\right) &= \mathrm{d}\overline{\kappa}_i\left(x\right) \\ &+ m\left(\int \omega\left(x,\xi\right) \mathrm{d}\overline{\kappa}_i\left(\xi\right) \mathrm{d}\xi - \mathrm{d}\overline{\kappa}_i\left(x\right)\right). \end{aligned} \tag{20}$$

Since the rate of the softening parameter is not known at the iteration beginning, some extra sub-iterations are required to solve Eq. (20) [40]. To simplify the calculations, the non-local rates were replaced by their approximations $\mathrm{d}\overline{\kappa}_i^{est}$ calculated based on the known total strain rate [32]

$$\begin{aligned} \mathrm{d}\widetilde{\kappa}_i\left(x\right) &\approx \mathrm{d}\overline{\kappa}_i\left(x\right) \\ &+ m\left(\int \omega\left(x,\xi\right) \mathrm{d}\overline{\kappa}_i^{est}\left(\xi\right) \mathrm{d}\xi - \mathrm{d}\overline{\kappa}_i^{est}\left(x\right)\right). \end{aligned} \tag{21}$$

The FE results show an insignificant influence of the calculation method of plastic rates of the non-local softening parameter [37]. In addition, an approximate method proposed by Brinkgreve [32] in Eq. (20) is less time consuming (by ca.30%).

As a weighting function ω_0 (called also an attenuation function or a non-local averaging function), the Gauss distribution was assumed [33]

$$\omega\left(r\right) = \frac{1}{c_g} e^{-\left(\frac{r}{l_c}\right)^2}, \tag{22}$$

where the parameter l_c is a characteristic length of micro-structure, r is a distance between two material points and c_g denotes a normalizing factor equal to $\sqrt{\pi} l_c$ (1D case), $\sqrt{\pi} l_c^2$ (2D case) and $\pi\sqrt{\pi} l_c^3$ (3D case). The averaging in Eq. (22) is restricted to a small representative area around each material point (the influence of points at the distance of $r = 3 \times l_c$ is only of 0.01%). A characteristic length is usually related to the micro-structure of concrete represented by the aggregate size. It is usually determined with an inverse identification process of experimental data. However, the determination of a representative characteristic length of micro-structure l_c is very complex in concrete since the strain localization can include a mixed mode (tensile zones and shear zones) and a characteristic length (which is a scalar value) is related to the fracture process zone with a certain volume which changes during a deformation (the width of the fracture process zone increases according to e.g. Pijaudier-Cabot et al. [41], but decreases after e.g. Simone [42]). In turn, other researchers conclude that the characteristic length is not a constant and it depends on the type of the boundary value problem and the current level of damage [43]. Based on our both numerical simulations of concrete and reinforced concrete beams under bending and experiments using a digital image correlation DIC technique in order to measure the width of a localized zone on the concrete surface [44–46], the characteristic length l_c of micro-structure was found to be about 5 mm in usual concrete (using the Gauss distribution function). A proper non-local transformation requires that a non-local field corresponding to a constant local field remains constant in the vicinity of a boundary. The applied weighting function satisfies the normalizing condition [33]

$$\omega\left(x,\xi\right) = \frac{\omega_0\left(\left\|x-\xi\right\|\right)}{\int_V \omega_0\left(\left\|x-\zeta\right\|\right) \mathrm{d}\zeta}. \tag{23}$$

The constitutive models where implemented into the Abaqus Standard program [15] with the aid of the subroutine UMAT (user constitutive law definition) and UEL (user element definition). For the solution of a non-linear equation of motion governing the response of a system of finite elements, a modified Newton-Raphson scheme was used (Section 2). The calculations were performed with a symmetric elastic global stiffness matrix instead of applying a tangent stiffness matrix (the choice was governed by access limitations to the commercial software Abaqus [15]. The procedure yielded sufficiently accurate and fast convergence. The magnitude of the maximum out-of-balance force at the end of each calculation step was smaller than 1% of the calculated total force on the specimen. To satisfy the consistency condition $f = 0$ in elasto-plasticity, the trial stress method (linearized expansion of the yield condition about the trial stress point) using

an elastic predictor and a plastic corrector with the return mapping algorithm [47] has been applied. The calculations were carried out using a large-displacement analysis. In this case, the actual configuration of the body is taken into account. The Cauchy stress was taken as the stress measure. The conjugate strain rate was the rate of deformation. The rotation of the stress and strain tensor have been calculated with the Hughes-Winget method [48]. A non-local averaging have been performed in the current configuration. This choice was governed by the fact that element areas in this configuration were automatically calculated by Abaqus [15]. The implicit dynamic analysis (including inertia forces) was used based on the Newmark method [15].

5. FE results for quasi-static cyclic and monotonic concrete tests

Due to the lack of accompanying monotonic and cyclic uniaxial laboratory tests, a general calibration procedure could not be applied to a coupled elasto-plastic-damage model. Therefore, the material constants were found by means of preliminary FE analyses in order to satisfactorily match numerical results with experimental ones.

5.1. Cyclic uniaxial compression and tension. First, a simple cyclic tension-compression-tension element test was calculated with the following constants: $\sigma_{yt0} = 4$ MPa, $\sigma_{yc0} = 40$ MPa, $H_p = E/2$ (H_p – hardening plastic modulus), $\phi = 20°$, $\psi = 10°$, $\beta = 550$, $\delta = 950$, $\kappa_0 = 8.5 \times 10^{-5}$, $\alpha = 0.95$, $\eta_1 = 1.2$, $\eta_2 = 0.15$, $a_t = 0.0$ and $a_c = 1.0$. The results of Figs. 1 and 2 show the different stiffness degradation during compression and tension (that is stronger in tension). A recovery of the compressive stiffness upon crack closure and un-recovery of the tensile stiffness as the load changes between tension and compression is satisfactorily reflected. Moreover, the tensile stiffness is not recovered when the load varies between compression and tension. For a better adjustment of the theoretical results to the experimental material behaviour, the scale factors should lie between 0 and 1. The evident difference between a pure damage model (without plastic strains) and coupled one (with plastic strains) during one uniaxial load cycle is demonstrated in Fig. 2.

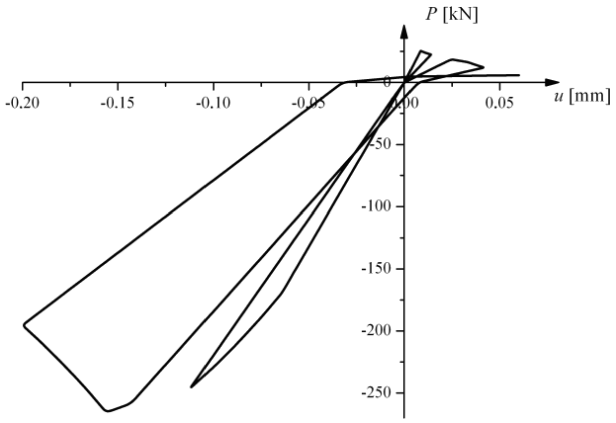

Fig. 1. Response of coupled elasto-plastic-damage constitutive model for concrete under cyclic tension-compression-tension test

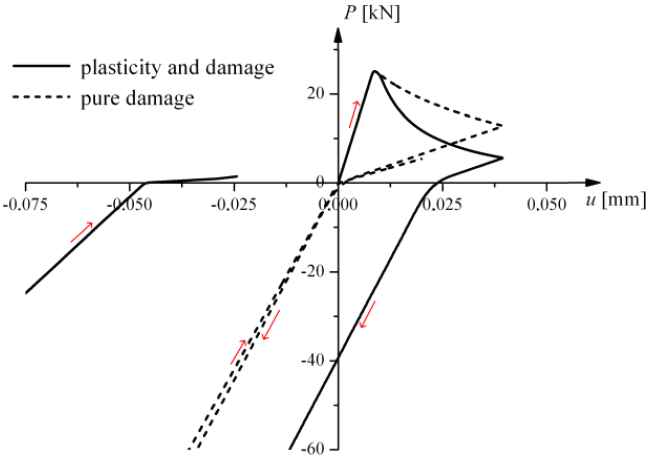

Fig. 2. Response of coupled elasto-plastic-damage constitutive model during tension-compression-tension test with and without plastic strain

The effect of the damage scale factors a_t and a_c on the load-displacement diagram under tension-compression-tension is described in Fig. 3 by assuming $a_t = 0.2$ and $a_c = 0.8$. This change of both factors is stronger in compression.

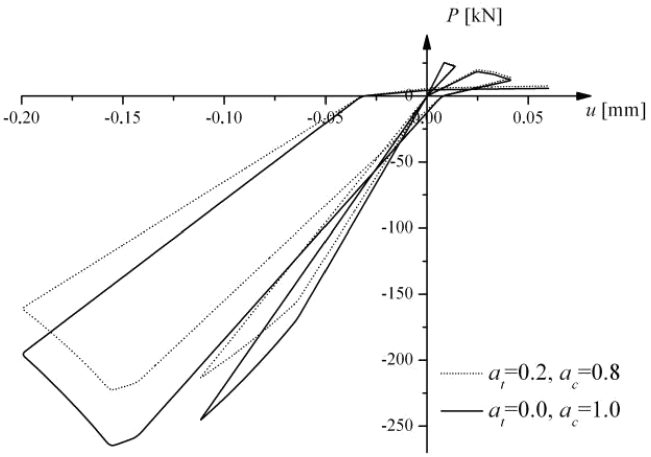

Fig. 3. Response of coupled elasto-plastic-damage constitutive model for concrete under tension-compression-tension test for different damage scale factors a_t and a_c

Finally, Fig. 4 demonstrates the 2D FE results with the coupled constitutive model for a concrete specimen subjected to uniaxial cyclic compression by taking strain localization into account. All nodes at the lower edge of a rectangular specimen were fixed in a vertical direction. The size of the specimen was arbitrarily chosen: 15 cm (height) and 5 cm (width). To preserve the stability of the specimen, the node in the middle of the lower edge was kept fixed. The deformations were initiated through constant vertical displacement increments prescribed to nodes along the upper edge of the specimen. The lower and upper edges were smooth.

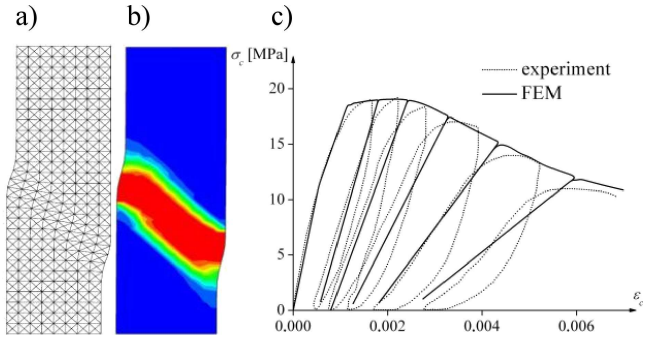

Fig. 4. Response of coupled elasto-plastic-damage constitutive model for concrete specimen under uniaxial cyclic compression from FE calculations (with damage scale factors a_t=0.0 and a_c=1.0): a) deformed FE mesh, b) contours of calculated non-local parameter, c) calculated and experimental [7] stress-strain curve

The number of triangular finite elements was 896 (the size of elements was not greater than $3\times l_c$ [11]). The material constants were: $E = 30$ GPa, $\nu = 0.18$, $\sigma_{yc} = 20$ MPa, $\phi = 25°$, $\psi = 10°$, $\eta_1 = 1.2$, $\eta_2 = 0.7$, $\delta = 800$, $l_c = 5$ mm, $a_t = 0.0$ and $a_c = 1.0$. To induce strain localization, a weak element was inserted in the middle of height, on edge of the specimen. The calculated stress-strain curve was qualitatively compared with the experimental one by Karsan and Jirsa [7].

The calculated stress-strain curve (Fig. 4c) is qualitatively the same as in a cyclic compressive experimental test [7] with respect to material softening and stiffness degradation. The calculated thickness of a localized zone is 3.4 cm ($6.8\times l_c$) and the inclination to the horizontal is about 45° (Fig. 4b). These results are very similar as those within elasto-plastic calculations [37]. The shear zone inclination is significantly higher (and more realistic) than this obtained with a simple non-local isotropic damage model [42], that was smaller than 35°–40°.

5.2. Four-point cyclic bending of notched concrete beams. The comparative 2D numerical simulations were performed with a concrete notched beam under four-point cycling bending subjected to the tensile failure [9]. The length of the beam was 0.5 m and the height 0.1 m. The deformation was induced by imposing a vertical displacement at two nodes at the top of the beam. In the calculations, the modulus of elasticity was $E = 40$ GPa, Poisson ratio $\nu = 0.2$ and characteristic length $l_c = 5$ mm. The concrete tensile strength in experiments was varied between $f_t = 2.49$ MPa and $f_t = 4.49$ MPa. The calculations were performed with 7634 triangular finite elements. The size of elements was not greater than $(2–3)\times l_c$ to obtain objective FE results [11, 37, 46].

The following constants were used in calculations $\sigma_{yt0} = 6.5$ MPa, $H_p = E/2$, $\kappa_0 = 4.3 \times 10^{-5}$, $\beta = 650$, $\alpha = 0.90$, $\eta_1 = 1.2$, $\eta_2 = 0.15$, $\delta = 450$, $a_t = 0$ and $a_c = 1$ (damage was based on elastic strains).

The calculated force-displacement curve (Fig. 5) exhibits good agreement with experimental outcomes. A calculated stiffness decrease is almost the same as in the experiment. The magnitude of a stiffness reduction is well reflected due to differentiation of the stiffness degradation under tension and compression. The calculated width of the localized zone above the notch is about 2.4 cm ($4.8 \times l_c$) (Fig. 5).

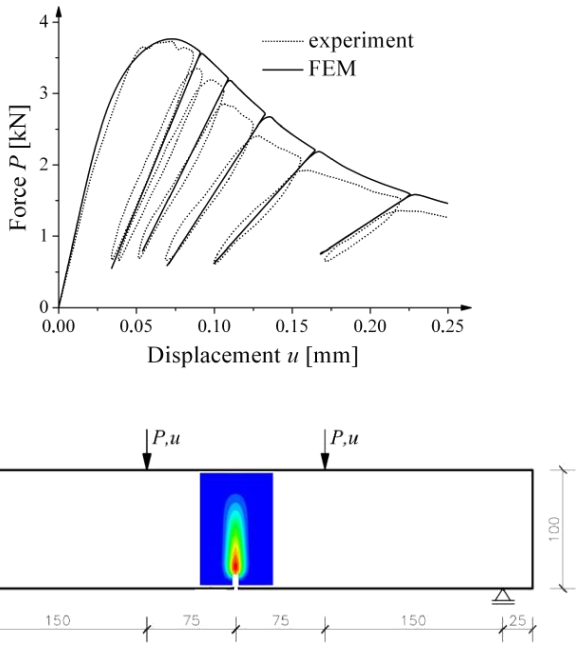

Fig. 5. The calculated load-displacement curve compared with experiment [9] and calculated localized zone above notch in concrete beam

5.3. Shear-tension failure of short reinforced concrete beam. The behaviour of short reinforced concrete beams with high longitudinal reinforcement and without stirrups subjected to the mixed shear-tension failure were simulated with the FEM. The results were compared with the corresponding laboratory tests carried out by Walraven and Lehwalter [49]. In experiments, the beam length L varied between 680 mm and 2250 mm and the height h was between 200 mm and 1000 mm (the beams' width b was always 250 mm). The cylinder compressive strength of concrete was about $f_c = 20$ MPa. In turn, the cylinder splitting tensile strength of concrete was about $f_t = 2$ MPa. The longitudinal reinforcement ratio of the specimens was 1.1% (yield strength was 420 MPa). The beams were incrementally loaded by a vertical force up to the peak applied at a mid-span of each beam. During loading, first, at about 40% of the failure load, bending cracks appeared. Afterwards, at about 45–50% of the failure load, the first inclined crack occurred. The beam failure took place in a gradual gentle way in shear compression by crushing concrete adjacent to the loading plate initiated by a formation of short parallel inclined cracks.

Based on preliminary calculations, the following constants were assumed for FE calculations: $\sigma_{y0} = 3.0$ MPa (tension), 30 MPa (compression), $H_p = E/2$, $\kappa_0 = 1.1 \times 10^{-4}$, $\beta = 150$, $\alpha = 0.90$, $\eta_1 = 1.1$, $\eta_2 = 0.65$, $\delta = 600$, $a_t = 0$ and $a_c = 1$ (damage was based on elastic strains, $l_c = 5$ mm).

The results with a coupled elasto-plastic-damage model for the beam with the height of $h = 400$ mm are given in Figs. 6 and 7.

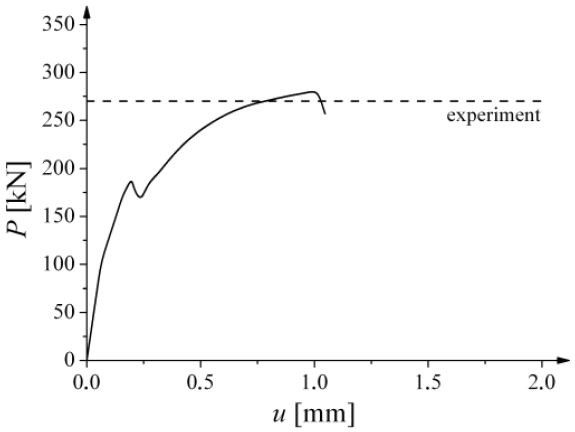

Fig. 6. Calculated force-displacement curve within coupled elasto-plasticity-damage as compared to experimental maximum vertical force for beam with height $h = 400$ mm)

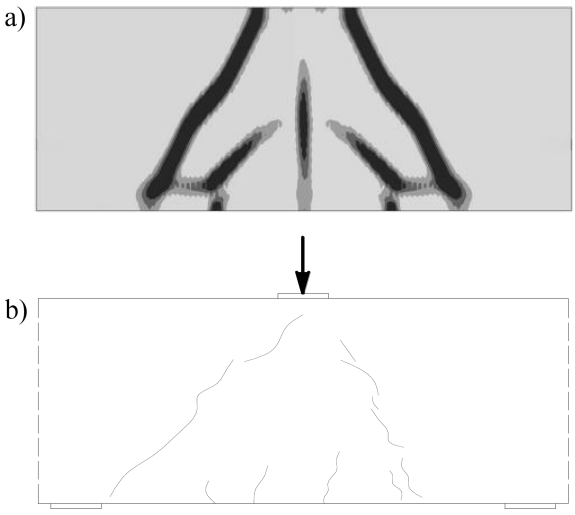

Fig. 7. Distribution of calculated non-local equivalent strain at failure within coupled elasto-plasticity-damage with non-local softening (a) against experimental crack pattern [49] (b) in concrete beam with height $h = 400$ mm

The calculated maximum vertical force is in a reinforced concrete beam in good agreement with the experimental value [49]. The maximum vertical forces differed by 3%–23% from the experimental ones in calculations with other beams (the highest difference was for the largest beam).

The calculated geometry of localized zones is also in satisfactory agreement with the experimental ones. At the beginning of a loading process the straight localized zones occur, next curved zones start to develop, finally the growth of high steep shear zones leads to failure.

Finally, Fig. 8 shows a comparison between the calculated and experimental deterministic size effect in beams: the shear stress $V/(bdf_c)$ at failure as a function of the effective beam depth. In addition, the size effect law by Bažant [1] is enclosed. The experimental, numerical and theoretical are similar and the beam strength shows strong size dependence on the beam height.

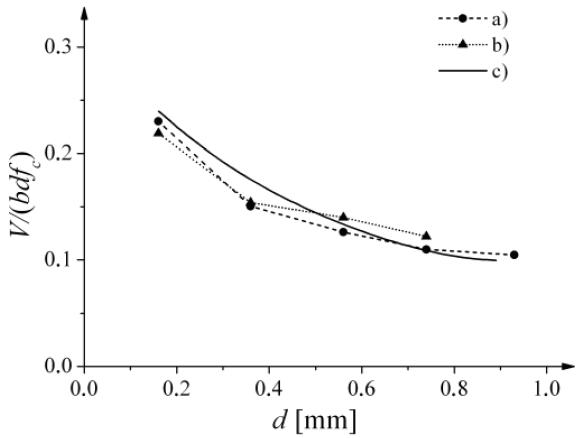

Fig. 8. Calculated size effect in short reinforced concrete beams from FE-analyses compared to experiments [49]) and to size effect law by Bažant [1] (b – beam width, d – effective beam height, f_c – compressive strength of concrete, V_u – ultimate vertical force): a) experiments, b) FE calculations, c) size effect law

6. Dynamic behaviour of concrete

6.1. Uniaxial compression. In numerical simulations, the homogeneous specimen was fixed at the lower and upper edge and the uniform vertical velocity was imposed along the upper boundary (Fig. 9).

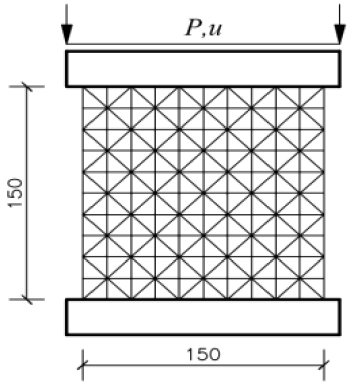

Fig. 9. Uniaxial compression test: specimen geometry, FE mesh and boundary conditions

The concrete parameters were: $E = 35.0$ GPa, $\nu = 0.15$, $\phi = 14°$, $\psi = 8°$, the compressive yield stress $\sigma_{yc0} = 30$ MPa with linear softening ($H = 1.55$ GPa). The relaxation time was equal to 1×10^{-6} s, 2×10^{-6} s, 1×10^{-5} s, 2×10^{-5} s and 2×10^{-4} s, respectively. The imposed strain rate was varied from $\dot{\varepsilon} = 10^{-5}$ 1/s up to $\dot{\varepsilon} = 10^{2}$ 1/s. In the first step, plane strain quasi-static calculations with the elastic-visco-plastic model and local softening were carried out for the different mesh discretization: 10×10, 20×20 and 40×40 (with plane strain triangular elements in the so-called "union jack pattern" and with plane strain four-node square elements with full integration). The FE calculations were performed without inertial forces during the so-called slow process (the prescribed vertical strain rate to the top edge was $\dot{\varepsilon} = 10^{-4}$ 1/s) and the fast process ($\dot{\varepsilon} = 1$ 1/s) (Figs. 10 and 11). The viscous parameter was $\tau = 2\times10^{-6}$ s.

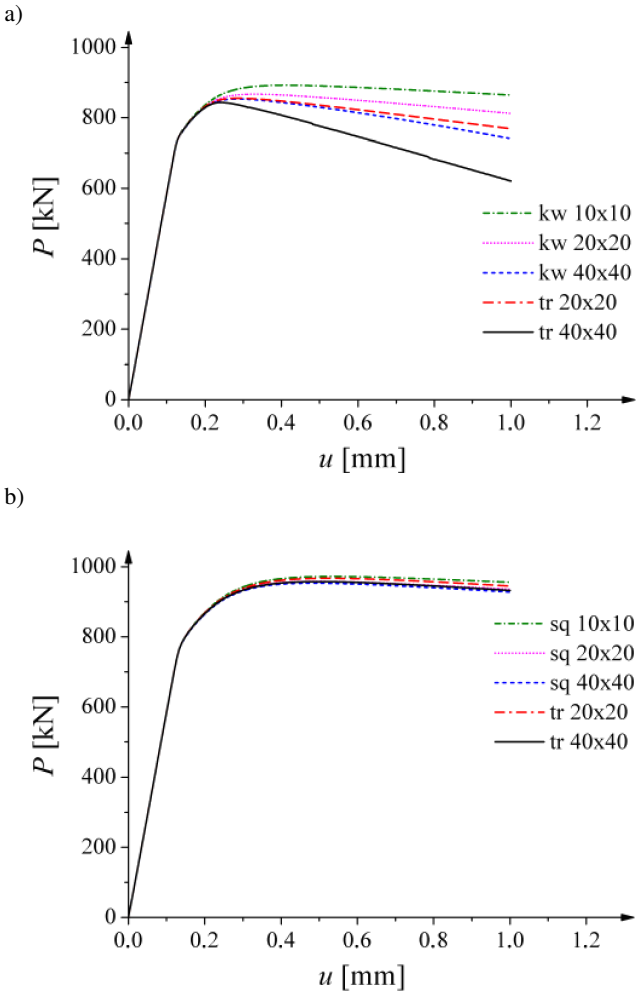

Fig. 10. The calculated force-displacement curves with elasto-visco-plastic model with local softening for different FE meshes: a) slow process ($\dot{\varepsilon} = 10^{-4}$ 1/s), b) fast process ($\dot{\varepsilon} = 1$ 1/s)

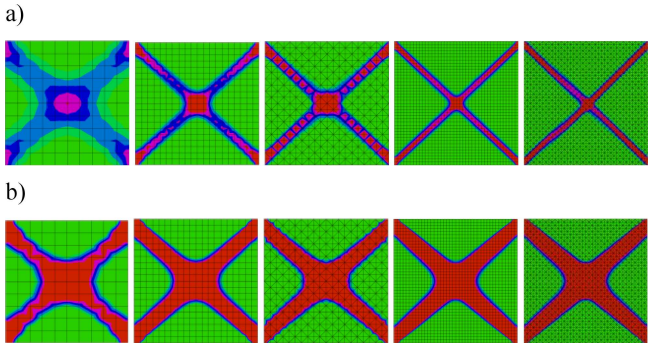

Fig. 11. The calculated contours of softening parameter with different meshes using elasto-visco-plastic model with local softening: a) slow loading process ($\dot{\varepsilon} = 10^{-4}$ 1/s), b) fast loading process ($\dot{\varepsilon} = 1$ 1/s)

The FE results of Figs. 10a and 11a are evidently mesh-dependent in a softening range during the slow process since the intersecting shear zones are confined to one row of finite elements and a different response in a post-peak regime was obtained for each mesh (Fig. 10a). Thus, the viscous terms are simply not sufficient to properly regularize the initial value problem. In turn, for the fast process, the mesh-dependence does not occur (Figs. 10b and 11b) and shear zones have larger widths than one element row. For all meshes, the width of the shear zone is very similar and equal to 22 mm (Fig. 11b). The numerical results (geometry of localized zones and force-displacement curves) are almost the same as in [4].

The effect of a non-local approach on FE quasi-static results within elasto-visco-plasticity is demonstrated in Figs. 12 and 13 ($\tau = 2 \times 10^{-6}$ s). Due to the presence of a characteristic length of micro-structure ($l_c = 5$–15 mm) in an inviscid phase, the widths of shear zones are also mesh-independent (wider than one row of elements) for the slow loading process (Fig. 12A). The width of a localized zone increases obviously with increasing l_c (Fig. 12A): 6.7 mm ($l_c = 0$ mm), 13.5 mm ($l_c = 5$ mm) and 24 mm ($l_c = 15$ mm). During fast loading process, the overlapping effect of both the non-locality and viscosity occurs. Thus, the width of localized zones increases: 22 mm ($l_c = 0$ mm), 25 mm ($l_c = 5$ mm), 31 mm ($l_c = 15$ mm) and their edges become smoother (Fig. 12B). In addition, a post-peak response exhibits smaller discrepancies (Figs. 13a and 13b).

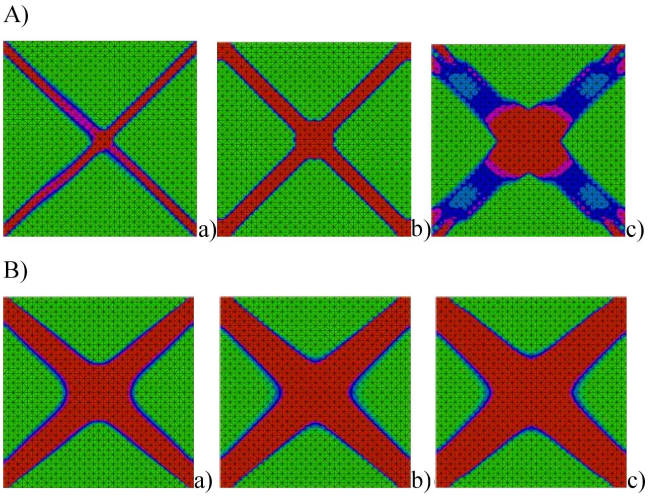

Fig. 12. The calculated contours of softening parameter for slow (A) and fast (B) loading process: a) elasto-visco-plastic model with local softening ($l_c = 0$ mm), b) elasto-visco-plastic model with non-local softening ($l_c = 5$ mm), c) elasto-visco-plastic model with non-local softening ($l_c = 15$ mm)

Next, the effect of several different strain rates $\dot{\varepsilon}$ ranged from 10^{-5} 1/s up to 100 1/s on the dynamic concrete behaviour was investigated (Figs. 14–16). The numerical strength results were compared with the compressive dynamic increase factor (CDIF) according to the CEB recommendations [50] based on laboratory experiments (in the form of a bilinear function of the factor CDIF of the strain rate $\dot{\varepsilon}$ in a logarithmic scale).

First, the dynamic FE results using the visco-plastic model (simulation #1, $\tau = 2 \times 10^{-5}$ s) and elasto-plastic model (simulation #2) with non-local softening ($l_c = 5$ mm) were compared during 2D and 3D calculations (Fig. 14). The calculated dynamic increase factor is underestimated as compared to CEB for the strain rate $\dot{\varepsilon} < 1$ 1/s (the same re-

sults were obtained at $\dot{\varepsilon} \leq 1$ 1/s). In turn, for high strain rates ($\dot{\varepsilon} > 10$ 1/s), the calculated dynamic increase factor is overestimated since material fragmentation is not taken into account. An increase of CDIF is more pronounced in real 3D simulations than in simplified 2D analyses. In simulations with viscosity, CDIF increases faster than in non-viscous simulations (at $\dot{\varepsilon} > 10$ 1/s).

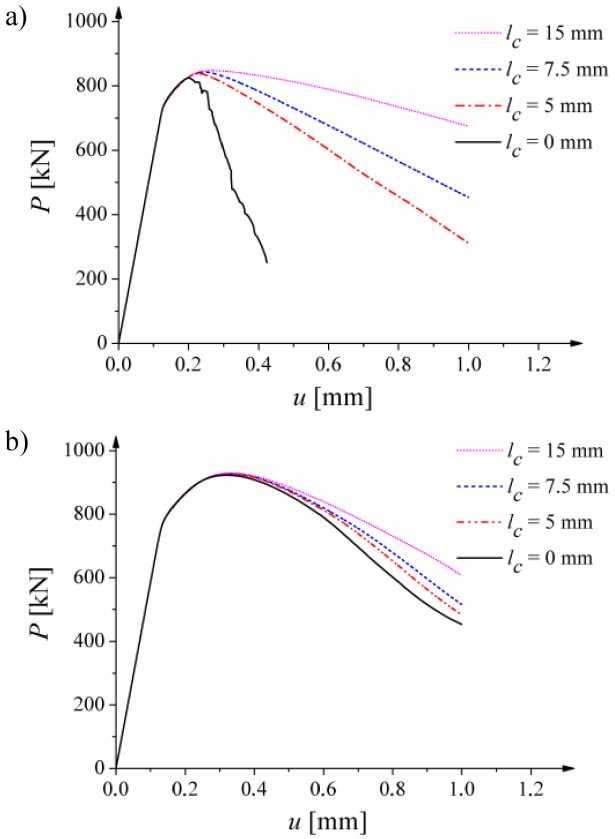

Fig. 13. Calculated force-displacement curves within elasto-visco-plastic model with non-local softening for different characteristic lengths of micro-structure: a) slow process ($\dot{\varepsilon} = 10^{-4}$ 1/s), b) fast process ($\dot{\varepsilon} = 1$ 1/s)

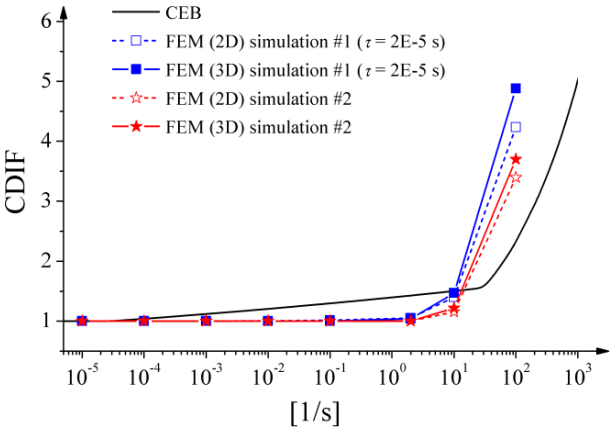

Fig. 14. Dynamic FE results considering effect of material formulation and viscosity with relaxation time $\tau = 2 \times 10^{-5}$ s as compared to dynamic compressive increase factor CDIF by CEB [50] (#1 – elasto-visco-plastic model with non-local softening and #2 – elasto-plastic model with non-local softening)

The shape and width (about 30 mm) of shear zones and load-displacement curves are practically the same at $\dot{\varepsilon} \leq 1$ 1/s (Figs. 15 and 16). The shape of localized zones starts to evidently change at $\dot{\varepsilon} > 10$ 1/s. For the highest strain rate $\dot{\varepsilon} = 100$ 1/s, the localized region is concentrated close to the upper surface (Fig. 15), and the material indicates a stiffer response in the elastic domain and a more brittle response in a softening range (Fig. 16).

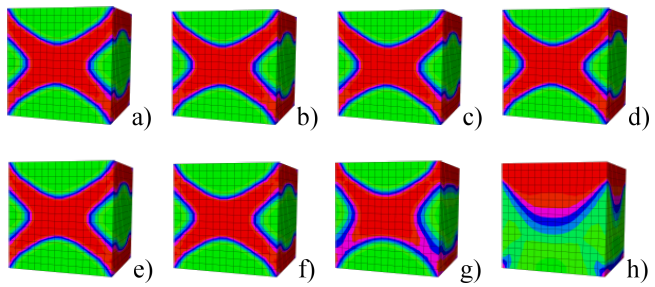

Fig. 15. The contours of non-local softening parameter from FE dynamic simulations for different vertical loading strain rates: a) 10^{-5} 1/s, b) 10^{-4} 1/s, 1/s, c) 10^{-3} 1/s, d) 10^{-2} 1/s, e) 10^{-1} 1/s, f) 10^{0} 1/s, g) 10^{1} 1/s, h) 10^{2} 1/s using elasto-visco-plastic model with non-local softening ($\tau = 1 \times 10^{-6}$ s, $l_c = 5$ mm)

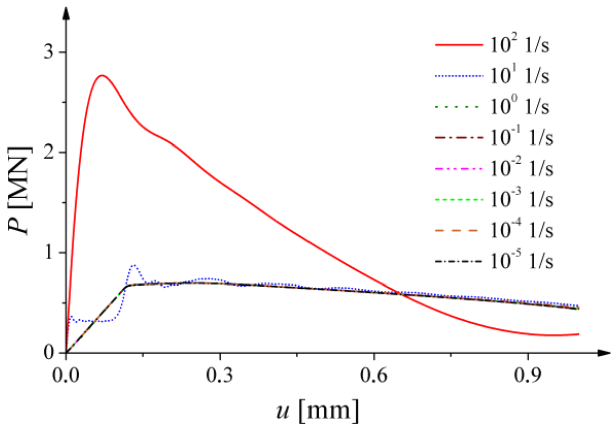

Fig. 16. The load-displacement curves from FE analyses for different vertical strain rate using elasto-visco-plastic model with non-local softening ($\tau = 1 \times 10^{-6}$ s, $l_c = 5$ mm)

6.2. Uniaxial tension. A dumbbell-shaped specimen was assumed as in the experiments by Yan and Lin [51] (Fig. 18). The following material parameters were assumed in FE calculations: $E = 29.0$ GPa, $\nu = 0.15$ and the tensile yield stress $\sigma_{yt0} = 2$ MPa with linear softening ($H = 0.65$ GPa). The numerical dynamic analyses were performed with the varying strain rate (10^{-5}–10^{1} 1/s).

Similarly as in uniaxial compression, the FE results show that the dynamic increase factor is underestimated as compared to the both experiments [51] and CEB recommendation [50] for the small strain rates $\dot{\varepsilon} < 1$ 1/s and overestimated for the large strain rates $\dot{\varepsilon} \geq 1$ 1/s a (Fig. 19). An increase of a viscosity parameter leads to a better accordance at $\dot{\varepsilon} < 1$ 1/s. For higher strain rates, the calculated dynamic factor is close to CEB with the very small viscosity parameter $\tau = 10^{-6}$ s

only. For simulations without viscosity, the strength's growth with increasing strain rate is not obtained.

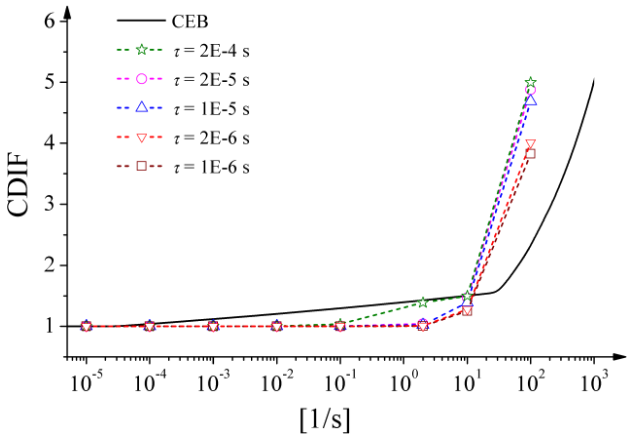

Fig. 17. Dynamic FE results of CDIF with different relaxation times τ as compared to CEB curve [50] (elasto-visco-plastic model with non-local softening)

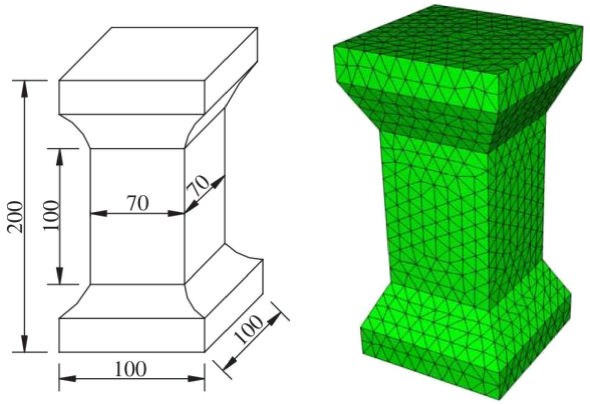

Fig. 18. Geometry of dumbbell-shaped specimen subject to uniaxial tension and FE mesh

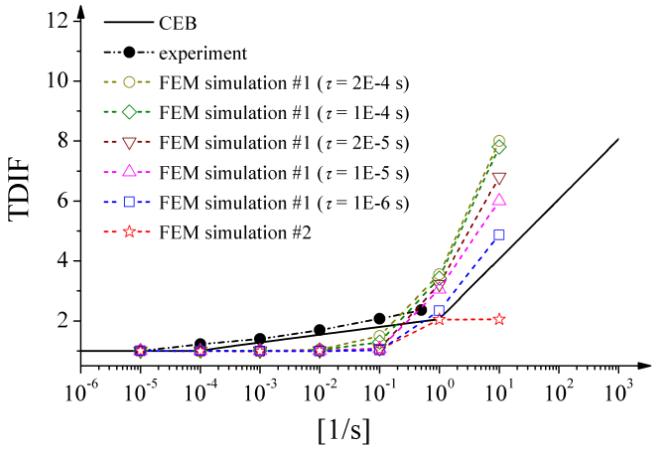

Fig. 19. Dynamic FE results of uniaxial tension as compared to TDIF by CEB [50] for different strain rates at different relaxation times (#1 – elasto-visco-plastic model with non-local softening and #2 – elasto-plastic model with non-local softening)

The numerical results with the elasto-visco-plastic model with non-local softening ($l_c = 5$ mm) and different viscosity parameters: $\tau = 1\times10^{-6}$ s, 1×10^{-5} s, 2×10^{-5} s, 1×10^{-4} s and 2×10^{-4} s (simulation #1) were compared with those with the elasto-plastic model with non-local softening ($l_c = 5$ mm) (simulation #2) (Figs. 19–21)

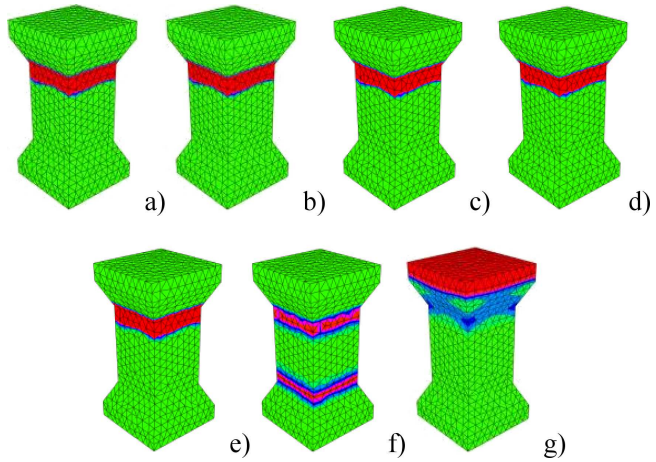

Fig. 20. The contours of non-local softening parameter from FE dynamic simulations for different strain rates $\dot{\varepsilon}$: a) 10^{-5} 1/s, b) 10^{-4} 1/s, c) 10^{-3} 1/s, d) 10^{-2} 1/s, e) 10^{-1} 1/s, f) 10^{0} 1/s, g) 10^{1} 1/s using elasto-visco-plastic model with non-local softening ($\tau = 1\times10^{-6}$, $l_c = 5$ mm)

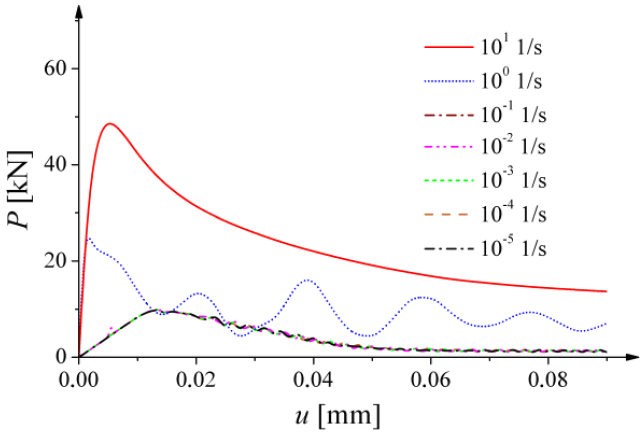

Fig. 21. The load-displacement curves from FE dynamic simulations for different strain rates $\dot{\varepsilon}$ using elasto-visco-plastic model with non-local softening ($\tau = 1\times10^{-6}$ s, $l_c = 5$ mm)

For slow strain rates ($\dot{\varepsilon} < 10^{-1}$ 1/s), a localized zone is created in the mid-region close to the specimen widening (the zone width is about 23 mm) (Fig. 20). For $\dot{\varepsilon} = 1$ 1/s two localized zone are created in the specimen mid-region with the width of 21 mm. In turn, at $\dot{\varepsilon} = 10^{1}$ 1/s, a localized zone is concentrated close to the specimen top. At $\dot{\varepsilon} > 1$ 1/s, the maximum vertical force significantly grows with increasing $\dot{\varepsilon}$ (Fig. 21).

7. Conclusions

The following conclusions can be derived from our FE analyses:

The FE quasi-static calculations demonstrate that our coupled elasto-plastic damage models enhanced by a characteris-

tic length of micro-structure in a softening regime can properly reproduce the experimental load-displacement diagrams and strain localization in plain and reinforced concrete elements under monotonic and cyclic loading. The model captures plastic strains and stiffness degradation in both tension and compression, and stiffness recovery effect during cyclic loading by means of a strain equivalence hypothesis. It is able to properly describe strain localization under both tension and compression due to a presence of a characteristic length of micro-structure. Its drawback is no clear distinction between elastic, plastic and damage strain rates, and a relatively large number of material constants to be calibrated. However, most of material constants may be calibrated independently with a monotonic uniaxial compression and tension (bending) test. Standard uniaxial cyclic tests are needed to calibrate damage scale factors.

A strengthening effect is obtained in FE dynamic simulations in concrete with our elasto-visco-plastic model and non-local softening at increasing strain rates under both compression and extension. The FE results may differ from the CEB recommendations based on the experimental outcomes. The calculated dynamic increase factor is namely too low at small strain rates and too high at high strain rates. The viscous terms in a plastic domain are not sufficient enough to properly describe creep and viscosity due to the water content. Thus, further research works on the formulation of a realistic coupled elasto-visco-plastic-damage model are needed by taking into account elastic viscosity [4] and material fragmentation [27].

Acknowledgements. Research work has been carried out within the project: "Innovative ways and effective methods of safety improvement and durability of buildings and transport infrastructure in the sustainable development" financed by the European Union. The numerical calculations were performed on super-computers of the Academic Computer Centre TASK in Gdańsk.

REFERENCES

[1] Z.P. Bažant and J. Planas, *Fracture and Size Effect in Concrete and Other Quasibrittle Materials*, CRC Press, London, 1998.

[2] J. Tejchman and J. Bobiński, *Continuous and Discontinuous Modeling of Fracture in Concrete Using FEM*, Springer, Berlin, http://dx.doi.org/10.1007/978-3-642-28463-2, 2013.

[3] P. Moonen, J. Carmeliet, and L.J. Sluys, "A continuous-discontinuous approach to simulate fracture processes", *Philosophical Magazine* 88, 3281–3298 (2008).

[4] A. Winnicki, "Viscoplastic and internal discontinuity models in analysis of structural concrete", *Habilitation Monograph*, Cracow University of Technology, Cracow, 2007.

[5] T. Jankowiak, "Failure criteria for concrete under quasi-static and dynamic loadings", *PhD Thesis*, Poznań University of Technology, Poznań, 2009, (in Polish).

[6] R.R. Pedersen, "Computational modelling of dynamic failure of cementitious materials", *PhD Dissertation*, TU Delft, Amsterdam, 2009.

[7] D. Karsan and J.O. Jirsa, "Behavior of concrete under compressive loadings", *J. Struct. Div. ASCE* 95 (ST12), 2543–2563 (1969).

[8] H.W. Reinhardt, H.A.W. Cornelissen, and D.A. Hordijk, "Tensile tests and failure analysis of concrete", *J. Struct. Eng. ASCE* 112, 2462–2477 (1986).

[9] D.A. Hordijk, "Local approach to fatigue of concrete", *PhD Thesis,* Delft University of Technology, Delft, 1991.

[10] J. Pamin and R. de Borst, "Stiffness degradation in gradient-dependent coupled damage-plasticity", *Arch. Mech.* 51 (3–4), 419–446 (1999).

[11] I. Marzec, J. Bobiński, and J. Tejchman, "Simulations of crack spacing in reinforced concrete beams using elastic-plasticity and damage with non-local softening", *Computers and Concrete* 4 (5), 377–403 (2007).

[12] T. Majewski, J. Bobiński, and J. Tejchman, "FE-analysis of failure behaviour of reinforced concrete columns under eccentric compression", *Eng. Structures* 30 (2), 300–317 (2008).

[13] J. Mazars, "A description of micro- and macroscale damage of concrete structures", *J. Engrg. Fracture Mech.* 25 (5/6), 729–737 (1986).

[14] M.G.D. Geers, "Experimental analysis and computational modeling of damage and fracture", *PhD Dissertation*, Eindhoven University of Technology, Eindhoven, 1997.

[15] *Abaqus Standard Users Manual Ver. 6.10*, Hibbitt, Karlsson & Sorensen, Inc, Rhode Island, 2011.

[16] J. Lee and G.L. Fenves, "Plastic-damage model for cyclic loading of concrete structures", *J. Eng. Mechanics* 124, 8, 892–900 (1999).

[17] I. Carol and K. Willam, "Spurious energy dissipation/generation in stiffness recovery models for elastic degradation and damage", *Int. J. Solids Structures* 33 (20–22), 2939–2957 (1996).

[18] P.H. Bischoff and S. H. Perry, "Compressive behaviour of concrete at high strain rates", *Mat. Struct.* 24, 425–450 (1991).

[19] D. Zheng and Q. Li, "An explanation for rate effect of concrete strength based on fracture toughness including free water viscosity", *Eng. Fracture Mechanics* 71, 2319–2327 (2004).

[20] X.X. Zhang, G. Ruiz, G. R.C. Yu and M. Tarifa, "Fracture behaviour of high-strength concrete at a wide range of loading rates", *Int. J. Impact Eng.* 36, 1204–1209 (2009)

[21] J. Ožbolt and H. W. Reinhardt, "Rate dependent fracture of notched plain concrete beams", *Proc. 7th Int. Conf. CONCREEP* 7, 57–62 (2005).

[22] L.J. Malvar and C.A. Ross, "Review of strain rate effects for concrete in tension", *ACI Materials J.* 95, 735–739 (1998).

[23] G. Gary, "Specific problems of concrete under large loading velocity", in *Scientific Report GRECO*, ed. J.M. Reynouard, GRECO, Paris, 1990, (in French).

[24] P. Rossi, "A physical phenomenon which can explain the mechanical behaviour of concrete under high strain rates", *Materials and Structures* 24, 422–424 (1991).

[25] D. Zheng and Q. Li, "An explanation for rate effect of concrete strength based on fracture toughness including free water viscosity", *Eng. Fracture Mechanics* 71, 2319–2327 (2004).

[26] X.X. Zhang, G. Ruiz, G.R.C. Yu, and M. Tarifa, "Fracture behaviour of high-strength concrete at a wide range of loading rates", *Int. J. Impact Eng.* 36, 1204–1209 (2009).

[27] S. Werner and K.-Ch. Thienel, "Influence of impact velocity on the fragment formation of concrete specimens", *Vortrag, Particles* 1, 211–221 (2011).

[28] U. Häußler-Combe and T. Kuehn, "Failure modeling of concrete with a novel strain rate sensitive viscoelastic retarded damage material formulation", *Eur. Congress on Computational Methods in Applied Sciences and Eng. (ECCOMAS 2012)* 1, CD-ROM (2012).

[29] L.J. Sluys, "Wave propagation, localization and dispersion in softening solids", *PhD Thesis*, Delft University of Technology, Delft, 1992.

[30] P. Perzyna, "Fundamental problems in viscoplasticity", *Advances in Applied Mechanics* 9, 243–377 (1966).

[31] G. Pijaudier-Cabot and Z.P. Bažant, "Nonlocal damage theory", *ASCE J. Eng. Mech.* 113, 1512–1533 (1987).

[32] R.B. Brinkgreve, "Geomaterial models and numerical analysis of softening", *PhD Thesis*, Delft University of Technology, Delft, 1994.

[33] Z.P. Bažant and M. Jirásek, "Nonlocal integral formulations of plasticity and damage: survey of progress", *J. Engng. Mech.* 128 (11), 1119–1149 (2002).

[34] C. Polizzotto, G. Borino, and P. Fuschi, "A thermodynamic consistent formulation of nonlocal and gradient plasticity", *Mech. Res. Communic*. 25, 75–82 (1998).

[35] G. Borino, B. Failla, and F. Parrinello, "A symmetric nonlocal damage theory", *Int. J. Solids Struct*. 40, 3621–3645 (2003).

[36] G.D. Nguyen, "A thermodynamic approach to non-local damage modelling of concrete", *Int. J. Solids and Structures* 45 (7–8), 1918–1934 (2008).

[37] J. Bobiński and J. Tejchman, "Numerical simulations of localization of deformation in quasi-brittle materials within nonlocal softening plasticity", *Computers and Concrete* 4, 433–455 (2004).

[38] M. Jirásek, "Nonlocal models for damage and fracture: comparison of approaches", *Int. J. Solids and Structures* 35 (31–32), 4133–4145 (1998).

[39] M. Jirásek and S. Rolshoven, "Comparison of integral-type nonlocal plasticity models for strain-softening materials", *Int. J. Eng. Science* 41 (13–14), 1553–1602 (2003).

[40] L. Strömberg and M. Ristinmaa, "FE-formulation of nonlocal plasticity theory", *Comput. Methods Appl. Mech. Engrg.* 136, 127–144 (1996).

[41] G. Pijaudier-Cabot, K. Haidar, and J.F. Dube, "Non-local damage model with evolving internal length", *Int. J. Num. and Anal. Meths. in Geomech*. 28, 633–652 (2004).

[42] A. Simone, "Continuous-discontinuous modelling of failure", *PhD Thesis*, Delft University, Delft, 2003.

[43] I. Ferrara and M. di Prisco, "Mode I fracture behaviour in concrete: nonlocal damage modeling", *ASCE J. Eng. Mechanics* 127 (7), 678–692 (2001).

[44] L. Skarżyński and J. Tejchman, "Calculations of fracture process zones on meso-scale in notched concrete beams subjected to three-point bending", *Eur. J. Mechanics/A Solids* 29, 746–760 (2010).

[45] L. Skarżyński, E. Syroka, and J. Tejchman, "Measurements and calculations of the width of the fracture process zones on the surface of notched concrete beams", *Strain*, 47, e319–e332 (2011).

[46] E. Syroka-Korol, "Experimental and theoretical investigations of size effects in concrete and reinforced concrete beams", *PhD Thesis*, Gdańsk University of Technology, Gdańsk, 2012.

[47] M. Ortiz and I.C. Simo, "An analysis of a new class of integration algorithms for elastoplastic constitutive relation", *Int. Num. Methods in Engrg.* 23, 353–366 (1986).

[48] T.J.R. Hughes and J. Winget, "Finite rotation effects in numerical integration of rate constitutive equations arising in large deformation analysis", *Int. J. Numerical Methods in Eng.* 15, 1862–1867 (1980).

[49] J. Walraven and N. Lehwalter, "Size effects in short beams loaded in shear", *ACI Structural J.* 91 (5), 585–593 (1994).

[50] L. Javier Malvar and J.E. Crawford, "Dynamic increase factors for concrete", *Twenty-Eighth DDESB Seminar* 1, CD-ROM (1998).

[51] D. Yan, G. Lin, "Dynamic properties of concrete in direct tension", *Cement and Concrete Research* 36, 1371–1378 (2006).